

physica status solidi (a) / Volume 219, Issue 2 / 2100577

Research Article | [Full Access](#)

Optimized Selective-Area p-Type Diffusion for the Back-Illuminated Planar InGaAs/InP Avalanche Photodiodes by a Single Diffusion Process

Yiren Chen, Zhiwei Zhang, Guoqing Miao, Hong Jiang, Hang Song✉

First published: 10 November 2021

<https://doi.org/10.1002/pssa.202100577>

Abstract

Herein, an alternative approach of selective-area zinc diffusion technique by single rapid thermal diffusion (RTD) using a $Zn_3P_2/Zn/SiO_2$ multilayer structure is proposed to realize p-type doping in the InP cap so as to fabricate planar InGaAs/InP avalanche photodiodes (APDs). Through the optimization of selective-area zinc diffusion in the InP cap, a low dark current, high responsivity, fast transient response, and high reliability near-infrared back-illuminated planar InGaAs/InP APD is obtained, which demonstrates a simple and efficient method for the development of high-performance planar InGaAs/InP APD focal plane arrays.

1 Introduction

The avalanche photodiodes (APDs) have been widely used as sensors and imagers in a broad range of military and civilian applications such as optical fiber communication, LiDAR 3D imaging, and quantum information processing, due to their competence in weak light detection.^[1-3] In the existing materials and devices, InGaAs/InP APDs distinguish themselves with superior performances such as high internal gain, high reliability, and high gain bandwidth in the near-infrared band (0.9–1.7 μm) with a separate absorption, grading, charge, and multiplication (SAGCM) heterostructure.^[4,5] In the structure, $In_{0.53}Ga_{0.47}As$ lattice-matched to InP substrate has been extensively used as the optical absorption layer while the unintentionally doped InP material used as the multiplication layer.^[5,6] It has been proven that planar InGaAs/InP APDs exhibited lower leakage current, higher stability, and higher reliability compared with mesa-type ones.^[7-9] Selective-area zinc diffusion technique has been thus developed as an effective way to obtain p-type InP layers for planar InGaAs/InP APDs.

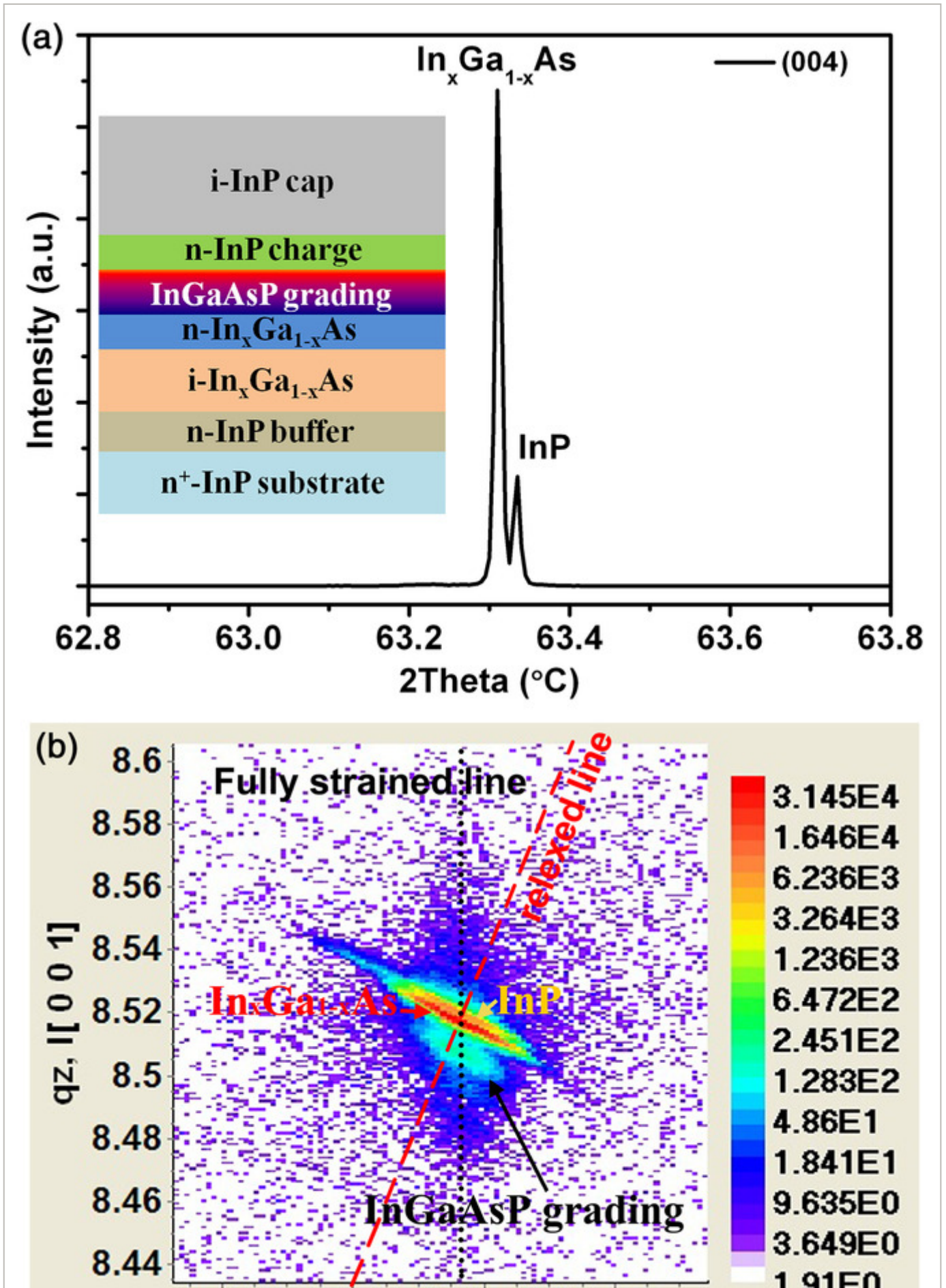
There were several methods to realize selective-area zinc diffusion in InP layers, mainly including chamber diffusion by metal-organic chemical vapor deposition (MOCVD) using dimethylzinc (DMZn) or diethylzinc (DEZn) as the p-type dopant^[10, 11] and furnace diffusion with ZnP₂ or Zn₃P₂ in a sealed or semiclosed or open quartz ampoule.^[12-14] The former has the disadvantages of high cost and risk of chamber pollution after external patterned processing for diffusion. The latter has the disadvantages of poor lateral uniformity, poor reproducibility, and limited wafer size.^[15]

In this article, for the purpose of improving the drawbacks mentioned above, a method of single rapid thermal diffusion (RTD) in N₂ atmosphere with a Zn₃P₂/Zn/SiO₂ multilayer structure is proposed, which provides the following advantages, namely, 1) simple operation; 2) steep diffusion interface resulted from fast heating and cooling speed; 3) easily obtaining high hole concentration at relatively low temperature due to the compensation of the metallic zinc film and the suppression of Zn₃P₂ vapor loss; and 4) no diffusion size limitation. Through this single diffusion method, the selective-area zinc diffusion in InP is optimized for fabricating a high-performance planar InGaAs/InP avalanche photodiode.

2 Experimental Section

2.1 Epitaxial Growth

The SAGCM heterostructure material shown in the inset of **Figure 1a** was grown on a commercial 2 in. (100)-oriented sulfur-doped InP (n⁺-InP) substrate by MOCVD (Aixtron 200/4) at a reactor pressure of 76 Torr. Trimethylgallium (TMGa), trimethylindium (TMIn), arsine (AsH₃), and phosphine (PH₃) were used as the precursors to epitaxy, with silane (SiH₄) as the n-type dopant. The epitaxial structure mainly consisted of a 1 μm-thick Si-doped n-InP buffer layer ($1.0 \times 10^{17} \text{ cm}^{-3}$), an In_xGa_{1-x}As absorption layer composed of a 2 μm-thick undoped In_xGa_{1-x}As and a 200 nm-thick Si-doped n-In_xGa_{1-x}As layer ($3.0 \times 10^{16} \text{ cm}^{-3}$), a lattice-matched InGaAsP grading layer with a total thickness of 120 nm, a 0.4 μm-thick Si-doped n-InP charge layer ($5.0 \times 10^{16} \text{ cm}^{-3}$), and a 3.5 μm-thick unintentionally doped InP cap layer in sequence. The InGaAsP grading layer has three 40 nm-thick step layers, and the corresponding photoluminescence wavelengths are evaluated to be 1.1, 1.3, and 1.5 μm, respectively. It alleviates the energy discontinuity between the n-In_xGa_{1-x}As layer and the n-InP charge layer and helps the hole carriers to transport through the heterogeneous interface rapidly.



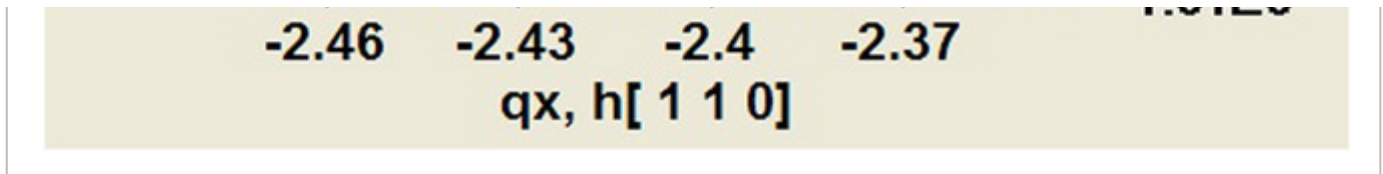


Figure 1

[Open in figure viewer](#) | [↓ PowerPoint](#)

Double-crystal X-ray diffraction images: a) the (004)-plane 2θ - ω scanning curve; b) the reciprocal space mapping around (115) plane. The material structure is shown in the inset of (a).

2.2 Device Fabrication

For planar InGaAs/InP APDs, the p-type layer to form the p-n junction was obtained by selective-area diffusion by single RTD using a $\text{Zn}_3\text{P}_2/\text{Zn}/\text{SiO}_2$ multilayer material as the dopant. The intuitive device fabrication flow can be referring to Figure S1, Supporting Information. In the process, a 200 nm-thick SiO_2 layer was first deposited on the InP cap layer by plasma-enhanced chemical vapor deposition (PECVD). A 35 μm square window and a 1 μm -wide guard ring window were opened on SiO_2 by standard photolithography and inductively coupled plasma (ICP) etching processes. The inner edge of the guard ring window was 5 μm away from the edge of the central square window. Then, a 100 nm-thick Zn_3P_2 film and a 50 nm-thick Zn film were deposited on the 200 nm-thick SiO_2 layer in sequence by thermal evaporation equipment. The zinc driven-in process was subsequently executed in N_2 atmosphere by a rapid thermal annealing (RTA) system under different conditions. After diffusion, the remaining Zn_3P_2 and Zn films were chemically removed by HNO_3 aqueous solution, followed by removal of SiO_2 layer by selective etching using HF solution of 20% concentration. In the subsequent process, a 200 nm-thick SiO_2 layer was once again deposited on the cleaned, zinc-diffused InP cap layer by PECVD and a 35 μm square window was opened on the diffusion region by the same process mentioned above. The zinc diffusion guard ring was buried under SiO_2 layer to form a floating guard ring. Finally, the p- and n-type electrodes were respectively fabricated by the standard photolithography, electron-beam evaporation, and lift-off processes. More specifically, a 20 μm square opening Ti/Pt/Au (50/20/200 nm) electrode was evaporated on the 35 μm square zinc-diffused InP cap to form the p-type electrical contact while a Ni/Ge/Au (50/20/200 nm) rectangular ring electrode is evaporated on the InP substrate side to fabricate a back-illuminated planar InGaAs/InP APD. During the whole diffusion process, another material used as a companion sample was simultaneously conducted the processes of deposition of $\text{Zn}_3\text{P}_2/\text{Zn}$ films, rapid thermal diffusion, and removal of $\text{Zn}_3\text{P}_2/\text{Zn}$ remains by HNO_3 aqueous solution, which was mainly used for electrochemical capacitance-voltage measurement to evaluate the p-type doping profile of the planar InGaAs/InP APD.

2.3 Characterization

A high-resolution X-ray diffractometer (HRXRD, Bruker D8) was adopted to characterize the (004) plane 2θ - ω scanning curve and the asymmetrical reciprocal space mapping (RSM) around the (115) reflection. The p-type doping profile was evaluated by electrochemical capacitance-voltage equipment (ECV, Nanometrics). The current-voltage (I - V) characteristics of the zinc-diffused InGaAs/InP APDs were measured by a semiconductor parameter analyzer (Agilent B1500A). A scanning electron microscope (SEM, Hitachi S4800) was used to characterize the cross-sectional morphology of the zinc-diffused InP. The spectral response characteristics were obtained by a spectral response test system equipped with a standard InGaAs-based photodetector as the calibration. The transient spectral response of the InGaAs/InP APD was stimulated by 10 Hz 1100 nm-wavelength laser using a tunable laser (Continuum, Horizon OPO) and recorded by a digital oscilloscope (Tektronix 5104).

3 Results and Discussion

The double-crystal X-ray diffraction images of the SAGCM heterostructure material before zinc diffusion are presented in Figure 1a,b. As can be seen from Figure 1a, two main peaks can be observed in the (004)-plane 2θ - ω scanning curve located at 63.32° and 63.34° , respectively. The former corresponds to the $\text{In}_x\text{Ga}_{1-x}\text{As}$ material and the latter corresponds to the InP material. The indium content (x) in the $\text{In}_x\text{Ga}_{1-x}\text{As}$ can be evaluated to be 53.6% by the joint of the Bragg's law, the Vegard law, and the interplanar spacing equation for cubic system given as following Equations (1-2)-(3)^[16, 17]

$$2d_{(hkl)} \sin \theta_{(hkl)} = n\lambda \quad (1)$$

$$d_{(hkl)} = a/(h^2 + k^2 + l^2)^{1/2} \quad (2)$$

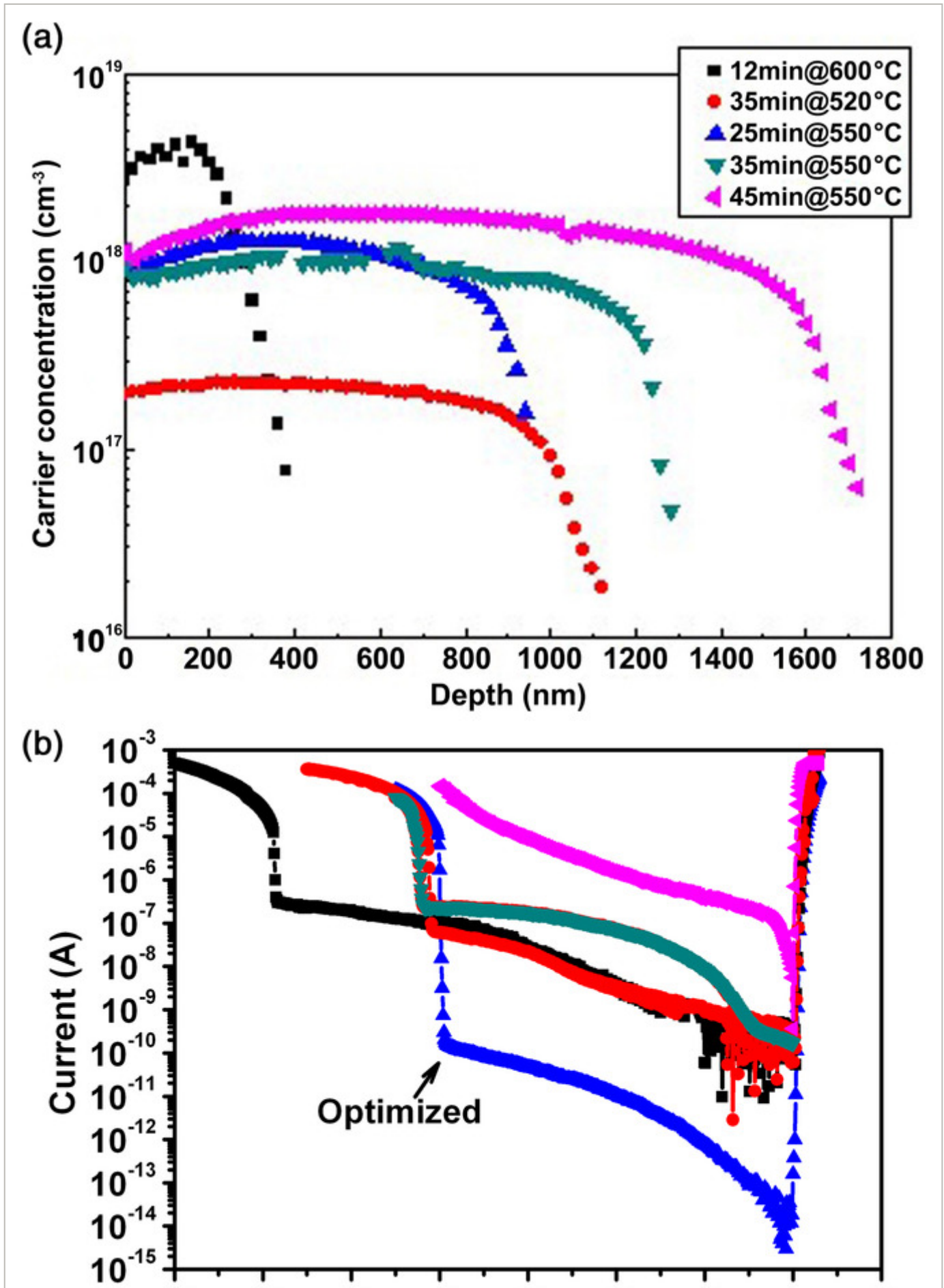
$$a_{\text{InGaAs}} = (1 - x)a_{\text{GaAs}} + xa_{\text{InAs}} \quad (3)$$

where h , k , and l represent the Miller indices of the diffraction plane. λ is the wavelength of the $\text{Cu K}\alpha_1$ radiation (0.15406 nm). $d_{(hkl)}$ and $\theta_{(hkl)}$ are on behalf of the interplanar spacing and the diffraction angle of (hkl) plane, respectively. a is the lattice constant of the cubic system. The lattice mismatch ratio between $\text{In}_x\text{Ga}_{1-x}\text{As}$ material and InP material also can be estimated to be 0.0283%, which means their lattices match perfectly during the epitaxy. To further understand the strain state in the epilayers, the asymmetrical RSM around the (115) reflection is performed, as shown in Figure 1b. The horizontal and vertical axes are stood for the

reciprocal lattice in the $[110]$ (q_x) and $[001]$ (q_z) directions. In the RSM image, there are mainly three diffracted peaks can be observed, corresponding to InP, InGaAs, and InGaAsP layers, respectively. They distribute along the q_z axis with the same in-plane lattice parameter, indicating a fully strained structure. This further confirms that the epitaxial layers are lattice-matching to the InP substrate. Therefore, assuming the grown material is isotropic and linear elastic, the strain of the epilayer (ϵ)_r can be evaluated by Equation (4),^[18] where ν is the Poisson's ratio of the material. a_s and a_L^\perp are the lattice parameter of substrate and the out-of-plane lattice parameter of the epilayer.

$$(\epsilon)_r = \left(\frac{1 - \nu}{1 + \nu} \right) \left(\frac{a_L^\perp - a_s}{a_s} \right) \quad (4)$$

To prepare planar InGaAs/InP APDs, the p-type layer to form the p–n junction is obtained by selective-area diffusion in the InP cap by single RTD using a Zn₃P₂/Zn/SiO₂ multilayer structure as the dopant. **Figure 2a** shows the p-type carrier concentration profiles in the InP caps by adjusting the diffusing temperature or diffusing time. As can be seen, the hole carrier concentration is determined by the diffusing temperature while the diffusing depth is determined by the time. Higher diffusing temperature results in higher hole carrier concentration in the InP cap. At the same diffusing temperature, the diffusing depth increases as the time prolongs. Due to the self-compensation mechanism, the hole carrier concentration saturates at approximately $5 \times 10^{18} \text{ cm}^{-3}$ for zinc-diffused p-type InP.^[10] Herein, we can obtain a concentration of about $4 \times 10^{18} \text{ cm}^{-3}$ at a diffusing temperature of 600 °C. Through comparing the typical I – V characteristics of p–n junctions after selective-area zinc diffusion at different conditions, we get the optimal sample as shown in **Figure 2b**, which is diffused at 550 °C for 25 min. Its diffusion depth of about 1 μm is evaluated by the companion sample using ECV method (**Figure 2a**). It should be noted that in order to reduce the edge breakdown, various planar type of APD structures, such as a shallow guard-ring structure^[19] and a double floating guard-ring structure,^[11, 20] have been developed by a double diffusion process. However, double diffusion process suffers from poor reproducibility.^[21, 22] Thus, herein, a single diffusion process with one floating guard-ring is implemented.



-70 -60 -50 -40 -30 -20 -10 0 10
Voltage (V)

Figure 2

[Open in figure viewer](#) | [↓ PowerPoint](#)

a) The carrier concentration profiles in InP wafers and b) the corresponding electrical properties of p–n junctions after single selective-area zinc diffusion at different conditions.

After the optimized diffusion in the InP cap, a back-illuminated planar InGaAs/InP APD is fabricated by the process mentioned in the Experimental Section. Its schematic and physical images are shown in **Figure 3a**. **Figure 3b** shows the cross-sectional image of the back-illuminated planar InGaAs/InP APD that confirms the diffusing depth strictly following the optimal result of **Figure 2**. The dark current and photocurrent as functions of bias voltage are shown in **Figure 4**. We define the breakdown voltage (about -40 V) at which the dark current reaches $10 \mu\text{A}$.^[23] The dark current is less than 0.1 nA when the bias voltage is up to 90% of the breakdown voltage. From **Figure 4**, we also can see that the 1550 nm-wavelength photocurrent and the dark current are almost completely coincident with each other when the bias voltage is higher than -20 V. This can be attributed to the fact that the depletion zone has not yet penetrated into the absorption layer, so that the photogenerated carriers in it cannot be driven to the multiplication layer. At about -20 V, the 1550 nm-wavelength photocurrent begins to increase due to the depletion edge extending to the absorption layer. Then, the 1550 nm-wavelength photocurrent increases abruptly, indicating the depletion in the absorption layer. At the punch-through voltage of -23 V, the absorption layer becomes completely depleted, and at the same time, the APD starts to produce an optical gain due to the avalanche impact ionization. The avalanche gain (M), defined as the difference between the primary multiplied current and the multiplied dark current normalized by the difference between the primary unmultiplied current and the unmultiplied dark current,^[24] is plotted in **Figure 4**. We get the unity gain ($M = 1$) at the punch-through voltage of -22.9 V and the gain ($M = 30$) at the 90% of breakdown voltage (-36 V). The avalanche gain is estimated to reach a maximum value of about 1200 at the breakdown voltage of -40 V.

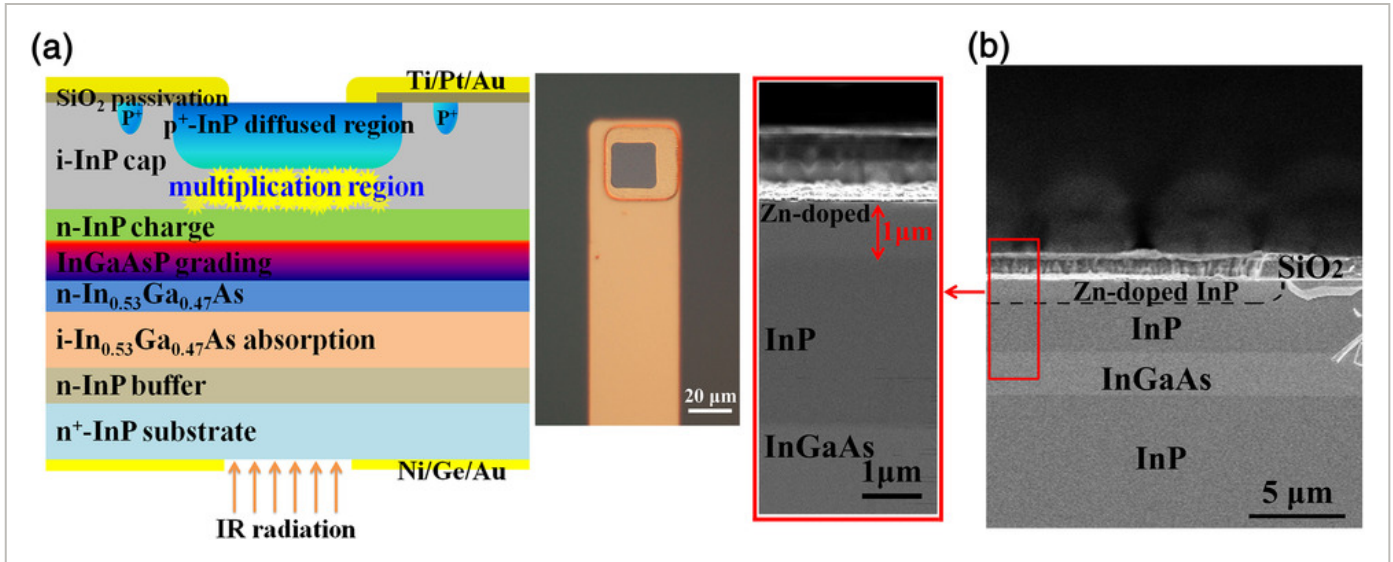


Figure 3

[Open in figure viewer](#) | [PowerPoint](#)

a) Schematic and physical images of the optimized back-illuminated planar InGaAs/InP APD and b) its SEM cross-sectional image.

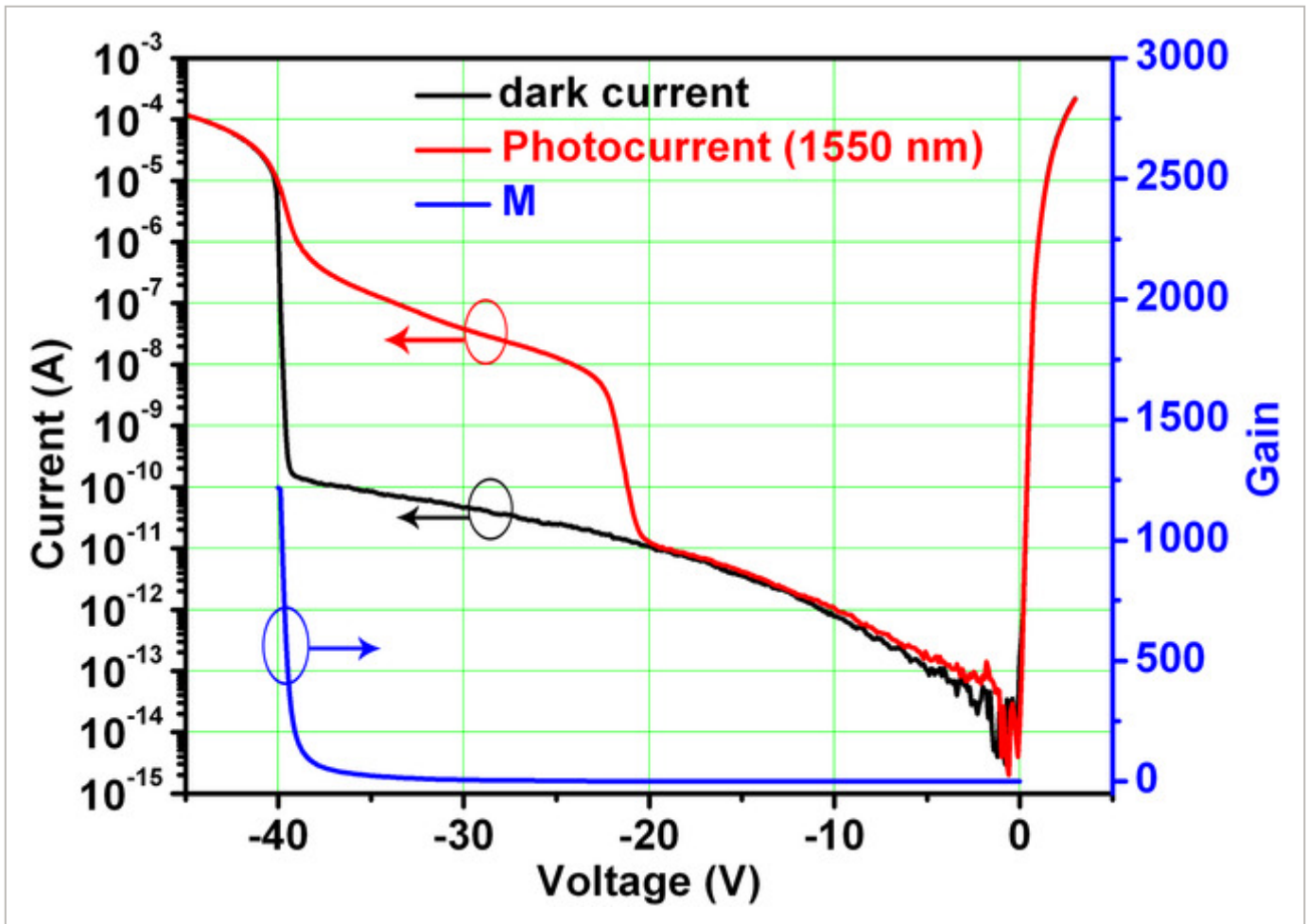


Figure 4

[Open in figure viewer](#) | [↓ PowerPoint](#)

The dark current and photocurrent as functions of bias voltage are shown on the left axis. The right axis indicates the gain.

In order to estimate the optical performance of the back-illuminated planar InGaAs/InP APD, the evolution of the spectral responsivity and corresponding external quantum efficiency (EQE) under different bias voltages is presented in Figure S2, Supporting Information, using a semilog scale (seen in Supporting Information). As can be seen from Figure S2a and b, Supporting Information, the response spectra are mainly ranging from 950 to 1700 nm, with enhanced responsivity as the reverse bias voltage increases. The growth rate of the responsivity and EQE keeps enlarging until sharply increasing near the breakdown voltage. It should be noted that the response spectrum of the InGaAs/InP APD can only be measured up to -36.6 V due to the input current limitation of the phase-locked amplifier in the system. The responsivity at 1.55 μm wavelength for our back-illuminated planar InGaAs/InP APD increases from 51 mA W^{-1} at 0 V to 455.5 A W^{-1} at -36.6 V, with a corresponding EQE increasing from 4% to $3.64 \times 10^4\%$. In **Figure 5**, it shows the spectral response curves at defined gain levels. Each of the spectral response curves is measured at a bias voltage in accordance with a typical avalanche gain value shown in **Figure 4**. The transient spectral response is also presented in **Figure 6**, in which the cyan line is on behalf of the synchronizing signal of the laser pulse with a frequency of 10 Hz while the yellow line represents the transient spectral response of the InGaAs/InP APD. As can be seen, it presents a 10–90% rise time of 8.825 ns and a 90–10% decay time of 38.75 ns under 36 V reverse bias (90% of breakdown voltage), which indicates its relatively good performance. The decay time slower than the rise time can be ascribed to the minority carrier lifetime determined by the physical processes such as relaxation, defect capture and release, etc.

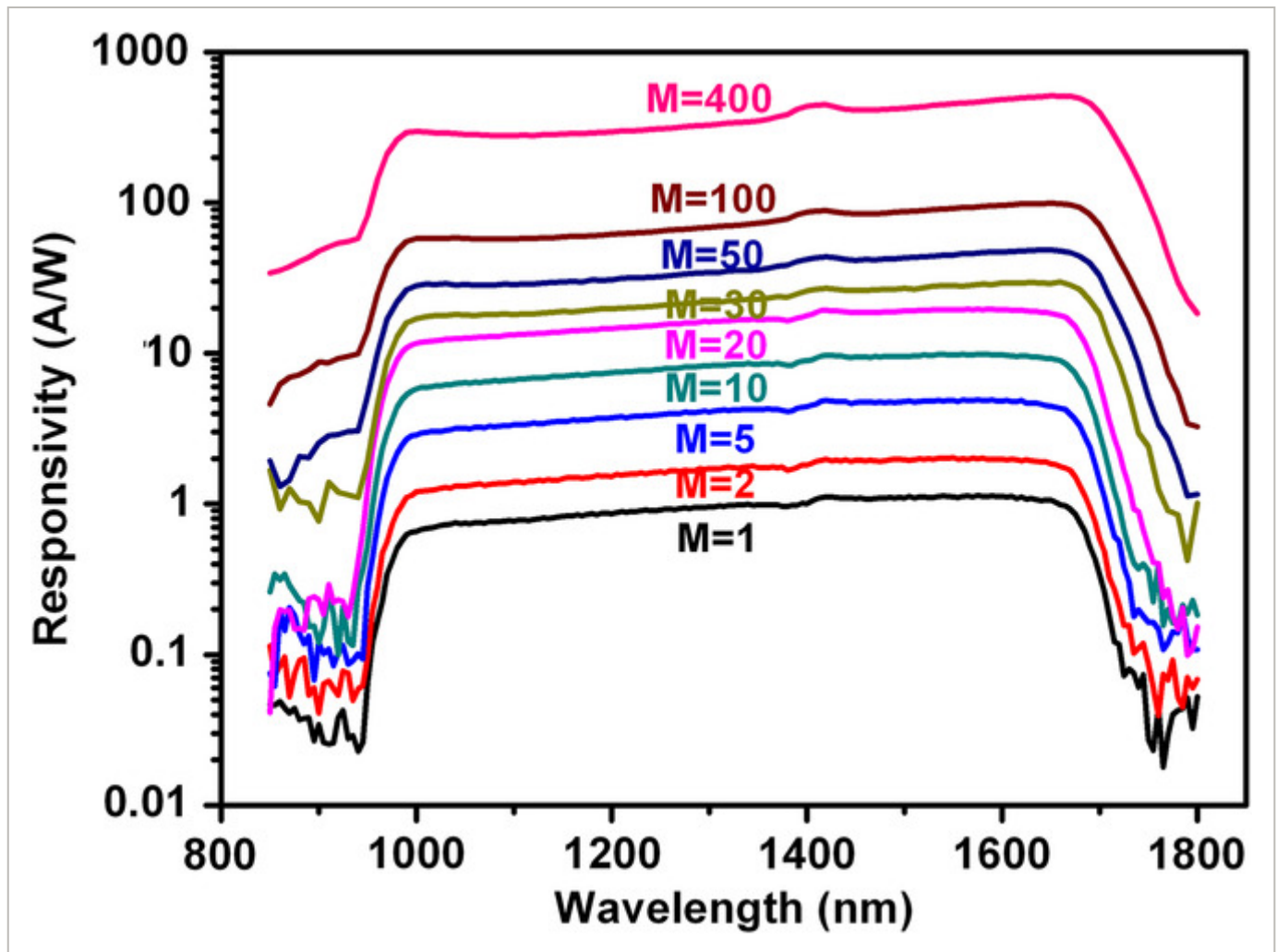


Figure 5

[Open in figure viewer](#) | [PowerPoint](#)

The spectral response curves at defined gain levels.

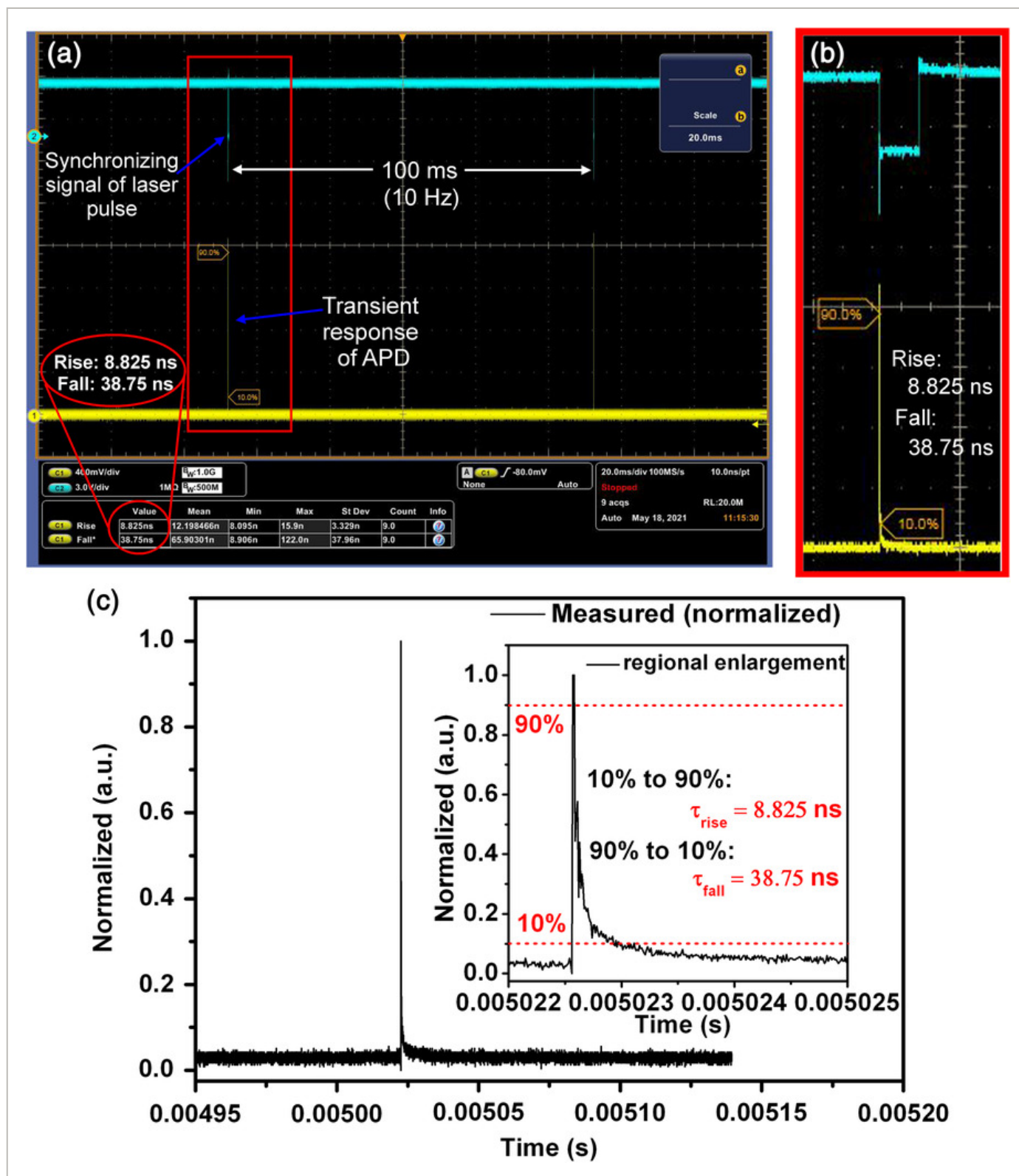


Figure 6

[Open in figure viewer](#) | [PowerPoint](#)

a) The transient spectral response under 36 V reverse bias. b) The enlargement of the red rectangle region in (a). c) The replotted curve for the normalized transient spectral response in (b). Its regional enlargement is shown in the inset.

4 Conclusion

In summary, the SAGCM heterostructure InGaAs/InP APD material is grown on a (100)-plane InP substrate with a slight lattice mismatch ratio of 0.0283% by MOCVD. To prepare planar InGaAs/InP APDs, a selective-area zinc diffusion technique by single RTD in N₂ atmosphere using a Zn₃P₂/Zn/SiO₂ multilayer structure is adopted to realize p-type doping in InP cap. A high-performance near-infrared planar InGaAs/InP APD is obtained by the optimal diffusion operating at 550 °C for 25 min with a diffusing depth of about 1 μm, which exhibits a low dark current of 0.1 nA at 90% of the breakdown voltage, an extremely high responsivity of 455.5 A W⁻¹ at -36.6 V before avalanche breakdown, and a fast transient response speed with a rise time of 8.825 ns and a decay time of 38.75 ns. These results demonstrate a simple and efficient method to achieve high-performance planar InGaAs/InP APDs.

Acknowledgements

Y.C. and Z.Z. contributed equally to this work. This work was supported by the National Key Research Program of China (grant no. 2018YFF0109801).

Conflict of Interest

The authors declare no conflict of interest.

Open Research



Data Availability Statement

The data that support the findings of this study are available in the supplementary material of this article.

Supporting Information



Filename	Description
pssa202100577-sup-0001-SuppData-S1.pdf 920.8 KB	Supplementary Material

Please note: The publisher is not responsible for the content or functionality of any supporting information supplied by the authors. Any queries (other than missing content) should be directed to the corresponding author for the article.

References



- 1 S. H. Kodati, S. Lee, B. Guo, A. H. Jones, M. Schwartz, M. Winslow, N. A. Pfeister, C. H. Grein, T. J. Ronningen, J. C. Campbell, S. Krishna, *Appl. Phys. Lett.* 2021, **118**, 091101.
[Crossref](#) | [CAS](#) | [Web of Science®](#) | [Google Scholar](#)

- 2 C. Bruschini, H. Homulle, I. M. Antolovic, S. Burri, E. Charbon, *Light Sci. Appl.* 2019, **8**, 87.
[Crossref](#) | [PubMed](#) | [Web of Science®](#) | [Google Scholar](#)

- 3 W.-H. Jiang, J.-H. Liu, Y. Liu, G. Jin, J. Zhang, J.-W. Pan, *Opt. Lett.* 2017, **42**, 5090.
[Crossref](#) | [CAS](#) | [PubMed](#) | [Web of Science®](#) | [Google Scholar](#)

- 4 R. Yang, *Proc. SPIE* 2021, **11763**, 117631Z.
[Google Scholar](#)

- 5 J. Zhang, M. A. Itzler, H. Zbinden, J. W. Pan, *Light Sci. Appl.* 2015, **4**, e286.
[Crossref](#) | [CAS](#) | [Web of Science®](#) | [Google Scholar](#)

- 6 S. P. Xi, Y. Gu, Y. G. Zhang, X. Y. Chen, L. Zhou, A. Z. Li, H. Li, *J. Cryst. Growth* 2015, **425**, 337.
[Crossref](#) | [CAS](#) | [Web of Science®](#) | [Google Scholar](#)

- 7 J. Burm, J. Y. Choi, S. R. Cho, M. D. Kim, S. K. Yang, J. M. Baek, D. Y. Rhee, B. O. Jeon, H. Y. Kang, D. H. Jang, *IEEE Photonics Technol. Lett.* 2004, **16**, 1721.
[Crossref](#) | [CAS](#) | [Web of Science®](#) | [Google Scholar](#)

- 8 O. J. Pitts, M. Hisko, W. Benyon, S. Raymond, A. J. Spring Thorpe, *J. Cryst. Growth* 2014, **393**, 85.
[Crossref](#) | [CAS](#) | [Web of Science®](#) | [Google Scholar](#)

- 9 P. Kleinow, F. Rutz, R. Aidam, W. Bronner, H. Heussen, M. Walther, *Phys. Status Solidi A* 2016, **213**, 925.
[Wiley Online Library](#) | [CAS](#) | [Google Scholar](#)

- 10 M. Islam, J. Y. Feng, A. Berkovich, P. Abshire, G. Barrows, F. Choa, *Proc. SPIE* 2016, **9819**, 98190G.
[Google Scholar](#)

-
- 11 O. J. Pitts, M. Hisko, W. Benyon, G. Bonneville, C. Storey, A. J. Spring Thorpe, *J. Cryst. Growth* 2017, **470**, 149.
[Crossref](#) | [CAS](#) | [Web of Science®](#) | [Google Scholar](#)
-
- 12 M. D. Kim, J. M. Baek, T. G. Kim, S. G. Kim, K. S. Chung, *Thin Solid Films* 2006, **514**, 250.
[Crossref](#) | [CAS](#) | [Web of Science®](#) | [Google Scholar](#)
-
- 13 G. Chen, M. Wang, W. Yang, M. Tan, Y. Wu, P. Dai, Y. Huang, S. Lu, *J. Semicond.* 2017, **38**, 124004.
[Crossref](#) | [Web of Science®](#) | [Google Scholar](#)
-
- 14 S. Feng, J. Hu, Y. Lu, B. V. Yakshinskiy, J. D. Wynn, C. Ghosh, *J. Electron. Mater.* 2003, **32**, 932.
[Crossref](#) | [CAS](#) | [Web of Science®](#) | [Google Scholar](#)
-
- 15 C.-C. Huang, C.-L. Ho, Y.-L. Lee, M.-C. Wu, *IEEE Electron Device Lett.* 2014, **35**, 1278.
[Crossref](#) | [CAS](#) | [Web of Science®](#) | [Google Scholar](#)
-
- 16 P. Rath, O. Kahl, S. Ferrari, F. Sproll, G. Lewes-Malandrakis, D. Brink, K. Ilin, M. Siegel, C. Nebel, W. Pernice, *Light Sci. Appl.* 2015, **4**, e388.
[Crossref](#) | [Web of Science®](#) | [Google Scholar](#)
-
- 17 Y. Zhao, D. Zhang, L. Qin, Q. Tang, R. H. Wu, J. Liu, Y. Zhang, H. Zhang, X. Yuan, W. Liu, *Opt. Express* 2011, **19**, 8546.
[Crossref](#) | [CAS](#) | [PubMed](#) | [Web of Science®](#) | [Google Scholar](#)
-
- 18 M. Choi, I.-Y. Jung, S. Song, C. S. Kim, *Mater. Sci. Semicond. Proc.* 2020, **120**, 105251.
[Crossref](#) | [CAS](#) | [Web of Science®](#) | [Google Scholar](#)
-
- 19 F. Acerbi, A. Tosi, F. Zappa, *Sensors Actuators, A* 2013, **201**, 207.
[Crossref](#) | [CAS](#) | [Web of Science®](#) | [Google Scholar](#)
-
- 20 S. Wang, Q. Han, L. Hou, H. Ye, Z. Lu, *Proc. SPIE* 2019, **10843**, 1084304.
[Google Scholar](#)
-
- 21 J. Jung, Y. H. Kwon, K. S. Hyun, I. Yun, *IEEE Photonics Technol. Lett.* 2002, **14**, 1160.
[Crossref](#) | [Web of Science®](#) | [Google Scholar](#)
-
- 22 K. Lee, K. Yang, *Phys. Status Solidi C* 2013, **10**, 1445.
[Wiley Online Library](#) | [CAS](#) | [Google Scholar](#)
-
- 23 M. A. Itzler, R. Ren-Michael, C. F. Hsu, K. Slomkowski, A. Tosi, S. Cova, F. Zappa, R. Ispasoiu, *J. Mod. Opt.* 2007, **54**, 283.

[Crossref](#) | [Web of Science®](#) | [Google Scholar](#)

24 A. Liu, J. Zhang, H. Xing, Y. Yang, *Appl. Opt.* 2019, **58**, 5339.

[Crossref](#) | [CAS](#) | [PubMed](#) | [Web of Science®](#) | [Google Scholar](#)

[Download PDF](#)

About Wiley Online Library

[Privacy Policy](#)

[Terms of Use](#)

[About Cookies](#)

[Manage Cookies](#)

[Accessibility](#)

[Wiley Research DE&I Statement and Publishing Policies](#)

[Help & Support](#)

[Contact Us](#)

[Training and Support](#)

[DMCA & Reporting Piracy](#)

[Opportunities](#)

[Subscription Agents](#)

[Advertisers & Corporate Partners](#)

[Connect with Wiley](#)

[The Wiley Network](#)

[Wiley Press Room](#)

Copyright © 1999-2022 John Wiley & Sons, Inc. All rights reserved